Numerical Modelling of Higher-Symmetric Periodic Structures with Hexagonal Lattice

Numerical Modelling of Higher-Symmetric Periodic Structures with Hexagonal Lattice

Martin Petek, *Graduate Student Member, IEEE,* José Rico-Fernández, *Graduate Student Member, IEEE,* Jorge Alberto Tobón Vásquez, *Member, IEEE,* Guido Valerio, *Senior Member, IEEE,* Francisco Mesa, *Fellow, IEEE,* Oscar Quevedo-Teruel, *Fellow, IEEE,* and Francesca Vipiana, *Senior Member, IEEE*

***Abstract*—This paper presents the development of the multi-modal transfer matrix method (MMTMM) to deal with periodic structures with hexagonal unit cells and higher symmetries. The method is able to calculate complex modal solutions, including the attenuation in the stopband. A key feature is the reformulation of the MMTMM into an eigenvalue problem whose eigensolutions in the complex plane can be systematically obtained for the boundaries of the irreducible Brillouin zone, where the phase-shift conditions are linearly dependent. The obtained phase-shift dispersion diagrams are verified against a commercial software, while the attenuation constant is validated with a developed method of moments. A glide-symmetric structure and a mirror half-turn structure are investigated. The latter is found to possess a highly isotropic stopband with a fractional bandwidth of 94.9%, wider than previously reported for holey structures. Finally, the operation of the unit cell is demonstrated with a practical implementation for preventing leakage in a waveguide flange.**

***Index Terms*—Electromagnetic bandgap materials, numerical analysis, periodic structure**

I. Introduction

PERIODIC structures have received significant attention in recent years. With the current shift towards higher frequencies in telecommunications [1], it is often necessary to integrate periodic structures, such as electromagnetic band gap (EBG) materials, into antennas. One way to improve the performance of periodic structures is to include higher symmetries, such as twist and glide symmetries [2], [3]. These symmetries were first studied in the 1960s [4], [5], [6], and have recently been investigated due to their appealing properties. For example, higher-symmetric metasurfaces have been used to produce lens [7], [8], and leaky wave antennas [9], [10], [11]. Another potential application is in the implementation of EBG materials. For this purpose, various types of unit cells have been proposed, such as holey structures [12], [13], [14], [15], pin structures [16], [17], mushrooms [18], and composite geometries [19].

In microwave/antenna engineering, most of the research on periodic structures has been focused on rectangular/square lattices. Recently, the use of hexagonal lattices in antenna designs has been explored [20], [21], [22], [23], then expanding earlier works on the subject [18], [24]. In [25], two different types of higher symmetries in hexagonal lattices have been investigated: the glide symmetry and the mirror half-turn (MHT) symmetry. In the former, the structure is invariant with respect to a mirroring and a translation of half a period; in the latter, the structure is invariant with respect to a mirroring and a rotation of π radians. Although [25] is the first reference to use the term "mirror half-turn symmetry", this symmetry was already studied in previous works [20], [26].

The electromagnetic modeling of periodic structures, and more specifically the calculation of their dispersion diagrams, can be carried out using different methodologies. In the literature, various modeling methods are accessible, well described, and applied. Typically, commercial eigenmode solvers are the preferred choice, but their main drawback is their inability to directly calculate the attenuation in the stopband. This feature is crucial to obtain a complete understanding of the characteristics of the stopband and essential information for the practical realization of the structure as an EBG [27]. Alternatively, mode matching [5], the rigorous coupled-wave analysis [28], the method of moments (MoM) [29], [30], and the multi-modal transfer matrix method (MMTMM) [27], [31], [32] have the ability to obtain the attenuation in the stopband. However, most of them have been focused on analysis of one-dimensional or two-dimensional Cartesian lattices.

In this work, we present a modeling procedure based on a novel implementation of the MMTMM, which can be used to obtain real and/or complex eigenmode solutions of structures with hexagonal lattices. The MMTMM is a hybrid method in which the coupling between multiple modes of the waveguide

This publication is based upon work from COST Action SyMat (CA18223), by the Horizon Europe Research and Innovation Program under the GENIUS Project, agreement no. 101072560, and in part by the project PON Research and Innovation "Microwave Imaging and Detection powered by Artificial Intelligence for Medical and Industrial Applications (DM 1062/21)," funded by the MUR. It is also supported by Unite! – University Network for Innovation, Technology and Engineering. The work of F. Mesa has been partially funded by the Grant PID2020-116739GB-I00 funded by MCIN/AEI/10.13039/501100011033. *(Corresponding author: Martin Petek.)*

Martin Petek, Jorge Alberto Tobón Vásquez and Francesca Vipiana are with Department of Electronics and Telecommunications, Politecnico di Torino, 10129 Torino, Italy (email: {martin.petek, jorge.tobon, francesca.vipiana}@polito.it)

José Rico-Fernández is with Northern Waves AB, SE-115 43 Stockholm, Sweden (e-mail: pepe.rico@northern-waves.com).

Guido Valerio is with Laboratoire de Génie Électrique et Électronique de Paris (GeePs), Sorbonne Université, 75252 Paris, France and with GeePs, Université Paris-Saclay, 91192 Gif-sur-Yvette, France (e-mail: guido.valerio@sorbonne-universite.fr).

Francisco Mesa is with the Department of Applied Physics 1, ETS Ingeniería Informática, Universidad de Sevilla, 41012 Seville, Spain (e-mail: mesa@us.es).

Oscar Quevedo-Teruel is with the Division for Electromagnetic Engineering and Fusion Science, KTH Royal Institute of Technology, SE-100 Stockholm, Sweden (e-mail: oscarqt@kth.se).

ports, placed at the boundaries of the structure, is obtained with a full-wave solver [31]. Here, CST Frequency Domain Solver (CST FDS) with hexahedral meshing is used [27], [31], [32], greatly reducing the effort required to implement the method. This choice of solver and meshing is employed because it allows to set ports having open boundary conditions on the corners of the structures. After the coupling matrices are obtained, they are reformulated as transfer matrices. The transfer matrix is used to create an eigenvalue problem that can be efficiently solved to calculate the complete dispersion diagram of the unit cell [32].

There are two challenges in implementing MMTMM for the analysis of hexagonal lattice structures. First, the use of the CST FDS with a hexahedral mesh requires the alignment of the waveguide ports with the Cartesian axes. Second, efficient linearized formulations MMTMM from [32] are not able to resolve all paths of the irreducible Brillouin zone. The first problem can be solved using supercells, while the second problem requires the development of a novel formulation of the MMTMM that results in a polynomial eigenvalue problem, proposed here for the first time.

The MMTMM method developed here is then used to analyze two holey structures: one having glide symmetry and one possessing MHT symmetry. We find that the MHT symmetric structure exhibits a wider stopband bandwidth in comparison to other periodic holey structures. Finally, we test the unit cell by manufacturing a flange spacer, additively manufactured using a laser powder-bed fusion technique. Preliminary numerical results on the glide-symmetric structure have been presented in a recent conference paper [33].

This work introduces a comprehensive and efficient modeling approach based on the the MMTMM to address the eigenproblem associated with periodic structures featuring a hexagonal lattice. The results are validated with an alternative MMTMM formulation and the method of moments [30]. Using the approach proposed by this paper, we thoroughly investigate the MHT geometry, which is found to improve the stopband bandwidth compared to the state of the art for holey structures [14].

This paper is organized as follows. In Section II, the chosen primitive unit cells and supercells and their corresponding irreducible Brillouin zones are presented. In Section III, the MMTMM and MoM modelings for hexagonal unit cells are described. Then, numerical results are presented in Section IV. The results of the experimental setup are presented in Section V. Finally, the conclusions and perspectives are given in Section VI.

II. Direct and Reciprocal Lattices

We analyze two distinct periodic structures consisting of a pair of parallel metallic plates separated by an air gap. The $z = 0$ plane is the middle plane between the two metallic surfaces. The metallic plates are partially carved with a hexagonal periodic pattern of circular holes with identical radii. The main difference between the two structures is the placement of the upper holes in relation to the lower ones. One structure features a symmetric arrangement of upper and lower holes that create a glide-symmetric configuration, while the other exhibits a MHT symmetry [25]. As shown in Figs. 1 and 2, the geometric parameters are the width of the hexagonal unit cell a, the separation between the upper and lower plates g, the radius of the hole r, and the depth of the hole h.

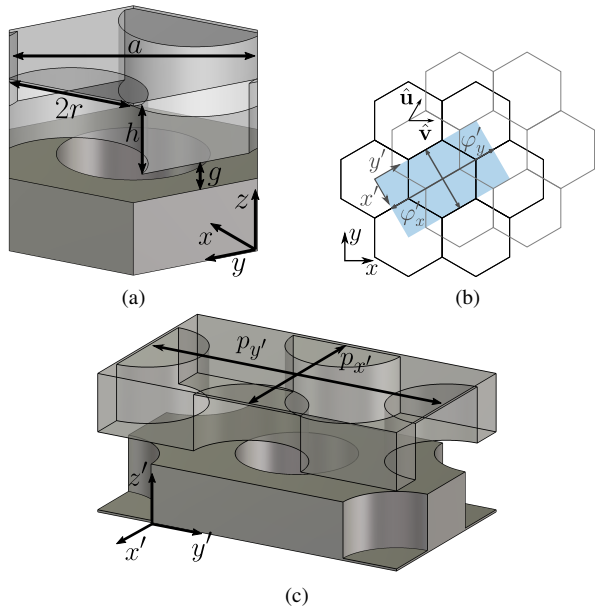

Fig. 1. Glide-symmetric geometry. (a) Primitive unit cell. (b) The hexagonal lattice, with the top plate in gray, depicts the glide-symmetric configuration. The chosen supercell is presented in a colored region. (c) Chosen supercell.

The hexagonal unit cell of the glide-symmetric structure is shown in Fig. 1(a). This structure is obtained by copy-mirroring the bottom perforated plate across the xy plane and translating it by half of a period $a/2$ along the two lattice vectors, $\hat{\mathbf{u}}$ and $\hat{\mathbf{v}}$, as shown in Fig. 1(b). Here, the top plate of the structure is colored gray, and a rectangular supercell is depicted in the colored region. A more clear view of this supercell is given in Fig. 1(c). The supercell is used for the MMTMM analysis and is chosen so that the paths in the irreducible Brillouin zone are aligned with the supercell coordinate axes as much as possible. This alignment simplifies the resolution with the MMTMM.

The unit cell of the MHT holey structure is depicted in Fig. 2(a). This configuration is obtained by copy-mirroring the bottom plate across the xy plane, and then rotating the upper part by π radians around $\hat{\mathbf{z}}$, centered on one of the vertices of the hexagon. This is shown schematically in Fig. 2(b). The corresponding rectangular supercell is shown in Fig. 2(c). Depending on the size of the holes, it may be necessary to slightly shift the cut of the chosen supercell structure in the y direction. This is to obtain a better homogeneity of the y-boundaries, as the CST FDS with hexahedral meshing's port-mode solver requires the structure to not significantly vary within the first three mesh-cells touching the port.

The glide-symmetric and MHT structures possess different symmetries in the xy-plane. Furthermore, the glide-symmetric structure possesses only two vertical planes where the structure is mirror-symmetric, while the MHT has three. As a result, the glide-symmetric structure has a larger irreducible Brillouin

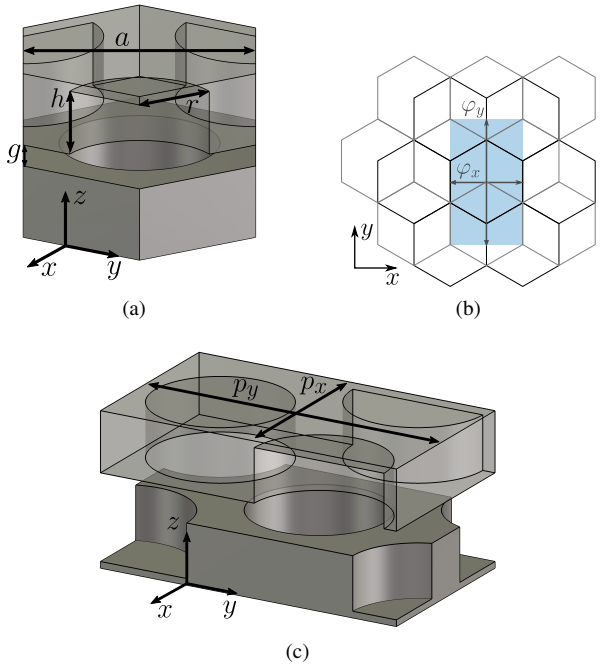

Fig. 2. MHT geometry. (a) Primitive unit cell. (b) The hexagonal lattice, with the top plate depicted in gray, represents a MHT symmetric configuration. The chosen supercell is presented in a colored region. (c) Chosen supercell.

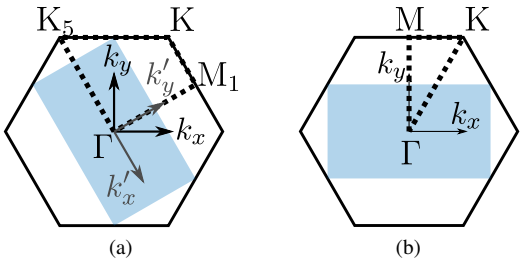

Fig. 3. First Brillouin zone of the analyzed geometries. The first Brillouin zone of the supercell is in the colored region, and the irreducible Brillouin zone is in the dashed region. (a) Glide-symmetric geometry. (b) MHT geometry.

zone, depicted in dashed lines in Fig. 3(a). The external hexagon of this figure is the first Brillouin zone of the primitive cell, with the corresponding Brillouin zone of the supercell of this glide-symmetric structure also colored blue in Fig. 3(a). The k_x and k_y are the components of the wavevector along the x and y axes. Since the glide-symmetric supercell is rotated by 60°, its corresponding Brillouin zone has its own associated wavevector coordinate system, k'_x and k'_y, which are aligned with x' and y' in Fig. 1(b).

To obtain information on the dispersion properties of periodic structures and, more specifically, on the stopband attenuation, it is necessary to scan the boundary of the irreducible Brillouin zone. The phases of the critical points of the supercells of the two structures studied in this work are reported in Table I.

III. Modelling Methodologies

Assuming a time-harmonic regime characterized by $e^{j\omega t}$, where ω represents the angular frequency, in this section we describe the methodologies employed to compute the dispersion diagrams of the structures under investigation.

TABLE I
PHASES OF THE SUPERCELL TO SCAN THE EDGES OF THE IRREDUCIBLE BRILLOUIN ZONE.

Glide-symmetric supercell

Point	φ'_x	φ'_y
Γ	0	0
K_5	$-\frac{4}{3}\pi$	0
K	$-\frac{2}{3}\pi$	2π
M_1	0	2π

MHT supercell

Point	φ_x	φ_y
Γ	0	0
M	0	2π
K	$\frac{2}{3}\pi$	2π

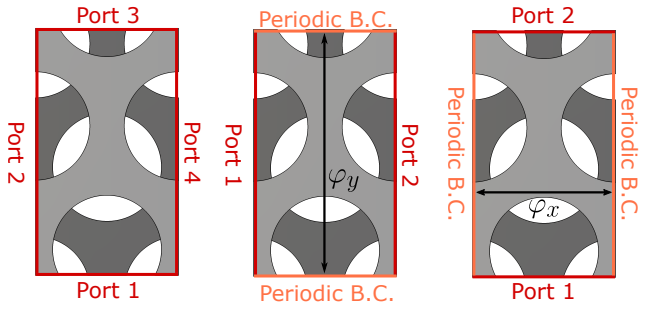

Fig. 4. Three simulation setups, illustrated with a top-down view of the analyzed supercell. (a) 2D-MMTMM approach with 4 ports surrounding the structure and open boundary conditions. (b) 1D-MMTMM approach, capable of obtaining only solutions of φ_x with a fixed φ_y, using only two ports and periodic boundary conditions. (c) 1D-MMTMM approach, capable of obtaining only solutions of φ_y with a fixed φ_x, using two ports only and periodic boundary conditions.

A. 2D Multimodal Transfer Matrix Method (2D-MMTMM)

The MMTMM is a hybrid method that, in a first step, employs full-wave solvers to resolve the coupling between port modes placed on the boundary of the structure [an example of these ports is given in Fig. 4(a)]. In this initial simulation, each port is defined to have $N_{\max}$ port modes with an open boundary condition defined at the x and y edges of the structure. The number $N_{\max}$ can be selected such that the highest cutoff frequencies of the port modes are well above the maximum frequency of interest. The coupling is then expressed in the form of the following frequency-dependent transfer matrix:

$$[\mathbf{T}] = \begin{bmatrix} [\mathbf{A}] & [\mathbf{B}] \\ [\mathbf{C}] & [\mathbf{D}] \end{bmatrix} \tag{1}$$

where the submatrices are obtained from the generalized scattering matrix via the equations presented, for instance, in [31]. Then, N port modes are selected in each port, with $N \leq N_{\max}$, the size of matrix $[\mathbf{T}]$ is $4N \times 4N$. Further discussion of the choice of port modes can be found in [31]. Once the transfer matrix has been obtained, an eigenproblem is set up as a post-processing procedure. Due to the periodicity of the structure, the multiplication of equivalent port voltages $\mathbf{V}_{x,y}$ and currents $\mathbf{I}_{x,y}$ with $[\mathbf{T}]$ is equal to the multiplication by an appropriate eigenvalue:

$$[\mathbf{T}] \begin{bmatrix} \mathbf{V}_x \\ \mathbf{V}_y \\ \mathbf{I}_x \\ \mathbf{I}_y \end{bmatrix} = \begin{bmatrix} \lambda_x \mathbf{V}_x \\ \lambda_y \mathbf{V}_y \\ \lambda_x \mathbf{I}_x \\ \lambda_y \mathbf{I}_y \end{bmatrix} . \tag{2}$$

Here, the subscripts x or y denote the Cartesian axes orthogonal to the ports. The eigenvalues λ_ν, with ν equal to x or y, can be expressed as

$$\lambda_\nu = \mathrm{e}^{-\mathrm{j}\varphi_\nu} = \mathrm{e}^{-\mathrm{j}k_\nu p_\nu} \tag{3}$$

where $\varphi_\nu = k_\nu p_\nu$ is the generalized phase shift with p_ν being the distance between two opposite ports. In general, the wavevector is a complex quantity that accounts for both the phase shift and attenuation in the structure. The system of equations in (2) is a nonlinear eigenvalue problem that can be linearized by fixing one of the eigenvalues, as presented in [32]. Then, the transfer matrix can be permuted to $[\widetilde{\mathbf{T}}]$ to write

$$[\widetilde{\mathbf{T}}] \begin{bmatrix} \mathbf{V}_x \\ \mathbf{I}_x \\ \mathbf{V}_y \\ \mathbf{I}_y \end{bmatrix} = \begin{bmatrix} \lambda_x \mathbf{V}_x \\ \lambda_x \mathbf{I}_x \\ \lambda_y \mathbf{V}_y \\ \lambda_y \mathbf{I}_y \end{bmatrix} . \tag{4}$$

If the permuted transfer matrix is written in terms of the following four submatrices:

$$[\widetilde{\mathbf{T}}] = \begin{bmatrix} [\widetilde{\mathbf{T}}_{xx}] & [\widetilde{\mathbf{T}}_{xy}] \\ [\widetilde{\mathbf{T}}_{yx}] & [\widetilde{\mathbf{T}}_{yy}] \end{bmatrix} \tag{5}$$

and we group the equivalent voltages and currents in the two vectors

$$\mathbf{F}_x = \begin{bmatrix} \mathbf{V}_x \\ \mathbf{I}_x \end{bmatrix} \qquad \mathbf{F}_y = \begin{bmatrix} \mathbf{V}_y \\ \mathbf{I}_y \end{bmatrix} \tag{6}$$

we obtain two linear eigenvalue problems depending on which eigenvalue is fixed,

$$\lambda_y \text{ fixed } \Rightarrow \big([\widetilde{\mathbf{T}}_{xx}] + [\widetilde{\mathbf{T}}_{xy}][\mathbf{Q}_y][\widetilde{\mathbf{T}}_{yx}]\big)\mathbf{F}_x = \lambda_x \mathbf{F}_x \tag{7}$$

$$\lambda_x \text{ fixed } \Rightarrow \big([\widetilde{\mathbf{T}}_{yy}] + [\widetilde{\mathbf{T}}_{yx}][\mathbf{Q}_x][\widetilde{\mathbf{T}}_{xy}]\big)\mathbf{F}_y = \lambda_y \mathbf{F}_y . \tag{8}$$

Here, the matrix $[\mathbf{Q}_\nu]$ is given by

$$[\mathbf{Q}_\nu] = \big(\lambda_\nu [\mathbf{I}] - [\widetilde{\mathbf{T}}_{\nu\nu}]\big)^{-1} \tag{9}$$

where $[\mathbf{I}]$ is the identity matrix. The size of the submatrices $[\widetilde{\mathbf{T}}_{\nu\nu}]$ is $2N \times 2N$, as well as that of resulting eigenvalue problems (7) and (8). The wavevector components can be computed from the eigenvalue via (3) with

$$k_\nu = \frac{1}{-\mathrm{j}p_\nu} \ln(\lambda_\nu) . \tag{10}$$

In the irreducible Brillouin zones shown in Fig. 3, there are some boundary paths where neither λ_x or λ_y can be fixed. In other words, there exist paths that are not aligned with the k_x or k_y axes. Therefore, it is not possible to utilize the linearization procedure for these paths of the Brillouin zone. This is the case for the paths $\overline{\mathrm{KK}_5}$ in the glide-symmetric structure and $\overline{\mathrm{K\Gamma}}$ in the MHT structure. The relationship between φ_x and φ_y for these sections is instead a linear function:

$$\varphi_y = n\varphi_x + \varphi_{y0} \tag{11}$$

with n being the slope and φ_{y0} the offset. By inserting (11) into (3), the eigenvalues are then expressed as

$$\lambda_y = \mathrm{e}^{-\mathrm{j}n\varphi_x} \mathrm{e}^{-\mathrm{j}\varphi_{y0}} = \lambda_x^n \lambda_{y0} . \tag{12}$$

Therefore, (4) can be rewritten as

$$\Big([\mathbf{M}_{n+1,x}]\lambda_x^{n+1} + [\mathbf{M}_{n,x}]\lambda_x^n + [\mathbf{M}_{1,x}]\lambda_x + [\mathbf{M}_{0,x}]\Big)\mathbf{F}_x = [\mathbf{0}] \tag{13}$$

with

$$[\mathbf{M}_{n+1,x}] = \lambda_{y0}[\widetilde{\mathbf{T}}_{xy}]^{-1} \tag{14}$$

$$[\mathbf{M}_{n,x}] = -\lambda_{y0}[\widetilde{\mathbf{T}}_{xy}]^{-1}[\widetilde{\mathbf{T}}_{xx}] \tag{15}$$

$$[\mathbf{M}_{1,x}] = -[\widetilde{\mathbf{T}}_{yy}][\widetilde{\mathbf{T}}_{xy}]^{-1} \tag{16}$$

$$[\mathbf{M}_{0,x}] = [\widetilde{\mathbf{T}}_{yy}][\widetilde{\mathbf{T}}_{xy}]^{-1}[\widetilde{\mathbf{T}}_{xx}] - [\widetilde{\mathbf{T}}_{yx}] . \tag{17}$$

The complete derivation of (13) and the relationship when the roles of x and y are switched are provided in the Appendix A. Equation (13) can now be used to scan two sections of the irreducible Brillouin zone in Fig. 3. The linear relationship (11) for these paths can be obtained from Table I. For example, according to (11), for $\overline{\mathrm{K\Gamma}}$ we have

$$n = \frac{\varphi_{y,\mathrm{K}} - \varphi_{y,\Gamma}}{\varphi_{x,\mathrm{K}} - \varphi_{x,\Gamma}} = \frac{2\pi - 0}{2\pi/3 - 0} = 3 \qquad \varphi_{y0} = 0 . \tag{18}$$

For $\overline{\mathrm{KK}_5}$ we find $n = 3$ and $\varphi_{y_0} = 2\pi$. Therefore, in both cases the relationship between the eigenvalues is $\lambda_y = \lambda_x^3$. This allows us to express (13) as the following polynomial eigenvalue problem:

$$\big([\mathbf{M}_{4,x}]\lambda_x^4 + [\mathbf{M}_{3,x}]\lambda_x^3 + [\mathbf{M}_{2,x}]\lambda_x^2 + [\mathbf{M}_{1,x}]\lambda_x\big)\mathbf{F}_x = -[\mathbf{M}_{0,x}]\mathbf{F}_x \tag{19}$$

where matrix $[\mathbf{M}_{2,x}]$ completes the matrix polynomial and is here null, $[\mathbf{M}_{2,x}] = [\mathbf{0}]$. The significance of this result is due to the availability of efficient routines for polynomial eigenvalue problems [34]. In this work, we solve the polynomial eigenvalue problem (19) by reformulating it into a generalized eigenvalue problem:

$$[\mathbf{Y}]\mathbf{F}_x = -[\mathbf{X}]\lambda_x \mathbf{F}_x \tag{20}$$

where the companion matrices are [35]

$$[\mathbf{Y}] = \begin{bmatrix} [\mathbf{M}_{3,x}] & [\mathbf{M}_{2,x}] & [\mathbf{M}_{1,x}] & [\mathbf{M}_{0,x}] \\ -[\mathbf{1}] & [\mathbf{0}] & [\mathbf{0}] & [\mathbf{0}] \\ [\mathbf{0}] & -[\mathbf{1}] & [\mathbf{0}] & [\mathbf{0}] \\ [\mathbf{0}] & [\mathbf{0}] & -[\mathbf{1}] & [\mathbf{0}] \end{bmatrix} \tag{21}$$

and

$$[\mathbf{X}] = \begin{bmatrix} [\mathbf{M}_{4,x}] & [\mathbf{0}] & [\mathbf{0}] & [\mathbf{0}] \\ [\mathbf{0}] & [\mathbf{1}] & [\mathbf{0}] & [\mathbf{0}] \\ [\mathbf{0}] & [\mathbf{0}] & [\mathbf{1}] & [\mathbf{0}] \\ [\mathbf{0}] & [\mathbf{0}] & [\mathbf{0}] & [\mathbf{1}] \end{bmatrix} . \tag{22}$$

The eigenvalue problem in (20) can be linearized with a matrix inversion:

$$-[\mathbf{X}]^{-1}[\mathbf{Y}]\mathbf{F}_x = \lambda_x \mathbf{F}_x \tag{23}$$

after which the standard eigenvalue problem can be easily solved using any of the available numerical libraries. After k_x has been obtained from (23) and (10), we can obtain k_y from (12), which can be rewritten as follows:

$$k_y = n\frac{p_x}{p_y}k_x + \frac{\varphi_{y0}}{p_y} . \tag{24}$$

For the supercells in this work, $p_x = a$ and $p_y = 2a\cos(\pi/6)$, therefore,

$$k_y = \sqrt{3}k_x \ . \tag{25}$$

This procedure is significantly more efficient and systematic than the search for zeros of the matrix determinant in the complex plane. The solution of the eigenproblem (23) has the same computational complexity as (7) or (8), but the matrix size is 4 times bigger. The proposed procedure does not make any assumption about the shape of the unit cells and can be utilized for other unit cells, including the square lattice, although the formulations derived from (13) are in general less stable than (7) and (8).

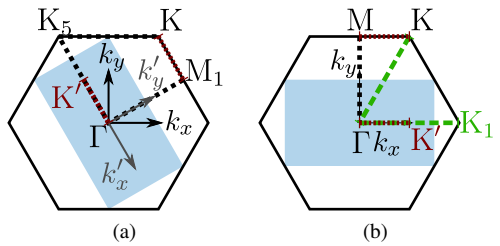

Fig. 5. Mirroring of paths in the 1D-MMTMM formulation. The first Brillouin zone of the primitive cell is within the hexagon and the colored region is the first Brillouin zone of the supercell. The dark red color depicts equivalence of paths outside the first Brillouin zone of the supercell to the paths within its first Brillouin zone. The light green color depicts equivalence of paths within the first Brillouin zone of the primitive cell. (a) Glide-symmetric structure. (b) MHT structure.

B. 1D Multimodal Transfer Matrix Method (1D-MMTMM)

Another approach, alternative to the four-port method outlined in the preceding Sect. III-A consists of replacing two opposite ports of the 2-D unit cell with an appropriate periodic boundary condition (PBC). With this procedure, we turn the initial 2-D problem into a 1-D problem, which is expected to be less computationally complex. In such an instance, it becomes essential to specify the phase shift of the two opposing ports with PBC's to make them correspond to the phase-shift conditions imposed by the segment of the Brillouin zone under examination. Here, we exploit two properties of Brillouin zones which are briefly described below:

1) Equivalence of paths when a supercell is used instead of a primitive cell. Since the periodic supercell is larger, its first Brillouin zone is smaller. Therefore, when a supercell is used, we obtain extra solutions that are mirrored from different regions, located in the first Brillouin zone of the primitive cell but outside the first Brillouin zone of the supercell [36]. An example of this is presented in Fig. 5(a) where the path $\overline{\Gamma \mathrm{K}'}$ is equivalent to $\overline{\mathrm{M}_1\mathrm{K}}$ for the glide-symmetric structure. In Fig. 5(b), the path $\overline{\mathrm{MK}}$ is equivalent to $\overline{\Gamma \mathrm{K}'}$ for the MHT structure.
2) Equivalence of paths due to the internal symmetries of the periodic structure [37]. These internal symmetries result in symmetries in the first Brillouin zone. For example, due to a 60 degree rotational symmetry in the MHT structure, the path $\overline{\Gamma \mathrm{K}}$ is equivalent to the path $\overline{\Gamma \mathrm{K}_1}$ in Fig.5(b).

We will now describe the method for determining the dispersion relations at the boundaries of the irreducible Brillouin zone for both unit cells. In the case of the glide-symmetric design, our goal is to study the path $\overline{\Gamma \mathrm{K}_5 \mathrm{K} \mathrm{M}_1 \Gamma}$. Each segment of this path can be treated in the following manner:

- Path $\overline{\Gamma \mathrm{K}_5}$: This path is resolved with the unit cell chosen in Fig. 1(c) with ports being placed as in Fig. 4(b), setting $\varphi'_y = 0$.
- Path $\overline{\mathrm{K}_5 \mathrm{K}}$: This path can be resolved by choosing a supercell such that it aligns with the Cartesian axes, as in Fig. 2(b). Then, we set up the simulation as in Fig. 4(b) with $\varphi'_y = 0$.
- Path $\overline{\mathrm{K}\mathrm{M}_1}$: The solutions for this segment are contained in the solutions for $\overline{\Gamma \mathrm{K}_5}$. Therefore, it is only necessary to properly extract the solutions from the first simulation of path $\overline{\Gamma \mathrm{K}_5}$.
- Path $\overline{\mathrm{M}_1 \Gamma}$: This path can be resolved by configuring the supercell simulation shown in Fig. 1(c) and applying the boundary conditions displayed in Fig. 4(c) with $\varphi'_x = 0$.

Consequently, it is necessary to conduct three separate simulations involving two ports using the 1D-MMTMM, rather than one simulation with four ports using the 2D-MMTMM.

For the MHT structure, we resolve the path $\overline{\Gamma \mathrm{M} \mathrm{K} \Gamma}$ as follows:

- Path $\overline{\Gamma \mathrm{M}}$: This path is resolved by using the supercell in Fig. 2(c), placing the ports as in Fig. 4(c) with $\varphi_x = 0$.
- Path $\overline{\mathrm{MK}}$: This path is resolved by using the supercell in Fig. 2(c), placing the ports as in Fig. 4(b) with $\varphi_y = 2\pi$.
- Path $\overline{\mathrm{K}\Gamma}$: The solutions for this path are contained in the simulation for $\overline{\mathrm{MK}}$, since setting $\varphi_y = 2\pi$ is identical to setting $\varphi_y = 0$ [note the equivalence of paths $\overline{\mathrm{MK}}$ and $\overline{\Gamma \mathrm{K}'}$ in Fig. 5(b)].

Consequently, it is necessary to perform two distinct simulations to study the boundaries of the irreducible Brillouin zone for the MHT configuration.

Taking the above considerations into account, the obtained scattering parameters are used to write the following standard eigenvalue problem:

$$[\mathbf{T}] \begin{bmatrix} \mathbf{V}_\nu \\ \mathbf{I}_\nu \end{bmatrix} = \lambda_\nu \begin{bmatrix} \mathbf{V}_\nu \\ \mathbf{I}_\nu \end{bmatrix} \tag{26}$$

where $[\mathbf{T}]$ is a $2N \times 2N$ transfer matrix. Since the above eigenvalue problem is linear, the eigenvalues λ_ν can easily be obtained using the available standard libraries. If there exist further symmetries in the geometry (for example, glide symmetry), it is possible to simulate only part of the unit cell following [38]. The main drawback of the 1-D approach is that varying the phase shift between the two opposed PBC's implies a new calculation of the corresponding transfer matrix through a full-wave simulation. Therefore, this formulation is best suited to find solutions where this phase shift is kept constant; as happens, for example, on the edge of the irreducible Brillouin zone. For isofrequency maps, it is better to use the formulation in (7)-(8).

C. Method of Moments (MoM)

An alternative to the MMTMM approaches described in Sections III-A and III-B is the MoM. This method will be mainly used in this work to validate the results of the MMTMM approaches that cannot be directly compared with those of full-wave simulators (namely, attenuation in the stopbands). For completeness, next we briefly outline our implementation of the MoM. For more in-depth information, we refer the reader to [30]. A given planar surface S of the unit cell of the periodic structure is modeled as a perfect electric conductor. The tangential electric field on this surface must be null, that is,

$$\mathbf{E}_{\tan}\{\mathbf{J}\} = -\mathrm{j}\omega\mathbf{A}_{\tan}\{\mathbf{J}\} - \nabla_S\Phi\{\mathbf{J}\} = \mathbf{0} \tag{27}$$

where $\mathbf{J}$ is the electric surface current density on S. The vector potential is computed with the following surface integral:

$$\mathbf{A}\{\mathbf{J}\} = \mu\int_S \boldsymbol{\mathcal{G}}(\mathbf{r},\mathbf{r}')\cdot\mathbf{J}(\mathbf{r}')\,\mathrm{d}S' \tag{28}$$

and the scalar potential with

$$\Phi\{\mathbf{J}\} = -\frac{1}{\mathrm{j}\omega\varepsilon}\int_S G(\mathbf{r},\mathbf{r}')\nabla'\cdot\mathbf{J}(\mathbf{r}')\,\mathrm{d}S' \tag{29}$$

with ε being the permittivity, μ the permeability, and $\mathbf{r}$ and $\mathbf{r}'$ the observation and source points, respectively. The dyadic Green's function is $\boldsymbol{\mathcal{G}}$, derived from its scalar counterpart G as shown, e.g., in [30]. In this work, we use two different Green's functions depending on the geometry of the structure. For the MHT structure, we discretize the entire primitive unit cell and use the standard free space periodic Green's function (FSPGF) given by [39]

$$G_{\mathrm{FSPGF}}(\mathbf{r},\mathbf{r}') = \sum_{m=-\infty}^{+\infty}\sum_{n=-\infty}^{+\infty}\mathrm{e}^{-\mathrm{j}\mathbf{k}_{\mathrm{t}00}\cdot\boldsymbol{\rho}_{mn}}\frac{\mathrm{e}^{-\mathrm{j}k_0R_{mn}}}{4\pi R_{mn}} \tag{30}$$

where $\mathbf{k}_{\mathrm{t}00}$ is the wavevector of the Floquet mode in the structure, k_0 is the free-space wavenumber, and R_{mn} is the distance between the observation and the m,n indexed source points in the lattice,

$$R_{mn} = \sqrt{(z-z')^2 + |\boldsymbol{\rho}-\boldsymbol{\rho}'-\boldsymbol{\rho}_{mn}|^2} \tag{31}$$

with

$$\boldsymbol{\rho}_{mn} = m\,\mathbf{s}_1 + n\,\mathbf{s}_2 \tag{32}$$

and $\mathbf{s}_1$ and $\mathbf{s}_2$ being the lattice periodicity vectors. In the hexagonal lattice, they can be defined as $\mathbf{s}_1 = a\hat{\mathbf{u}}$ and $\mathbf{s}_2 = a\hat{\mathbf{v}}$ [see Fig. 1(b)].

For the glide-symmetric structure, we use the higher-symmetric periodic Green's function (HSPGF) [30], which reduces the computational domain to only the bottom part of the structure. The contribution of the upper part of the structure, G_{T}, can be obtained by combining the FSPGF and the generalized Floquet theorem [6],

$$G_{\mathrm{T}}(\mathbf{r},\mathbf{r}') = \mathrm{e}^{-\mathrm{j}\mathbf{k}_{\mathrm{t}00}\cdot\boldsymbol{\rho}_{\mathrm{g}}}\,G_{\mathrm{FSPGF}}(\mathbf{r},\mathbf{r}'+\boldsymbol{\rho}_{\mathrm{g}}+2z'\hat{\mathbf{z}}) \tag{33}$$

with $\boldsymbol{\rho}_{\mathrm{g}}$ being the translation operation of the top plate,

$$\boldsymbol{\rho}_{\mathrm{g}} = 0.5\mathbf{s}_1 + 0.5\mathbf{s}_2\,. \tag{34}$$

TABLE II
OPTIMAL PARAMETERS FOR THE STUDIED UNIT CELLS

Parameter	Description	Glide	MHT
a	width of hexagon	8.7 mm	2.8 mm
r	radius of hole	$0.31a$	$0.38a$
h	depth of hole	$0.6a$	$0.6a$
g	gap	0.05 mm	0.05 mm

The complete scalar Green's function for glide-symmetric structures is then given by

$$G^{\pm}(\mathbf{r},\mathbf{r}') = G_{\mathrm{FSPGF}}(\mathbf{r},\mathbf{r}') \pm G_{\mathrm{T}}(\mathbf{r},\mathbf{r}') \tag{35}$$

where both $+$ and $-$ choices must be explored when searching for solutions, as they correspond to different modal field configurations [30].

IV. NUMERICAL RESULTS

In this section, we present the numerical results of the methods described in Sect. III. To properly assess the usability of individual unit cells and compare the results with the recently proposed three-hole structure [14], we set the lowest bound of the stopband approximately at 30 GHz and optimize the parameters that maximize the stopband. These values are provided in Table II. The gap between the top and bottom plate, g, is fixed to 0.05 mm for consistency with previous work [14], [27]. For the real part of the dispersion diagram (frequency versus phase shift), the three methods 2D-MMTMM, 1D-MMTMM, and MoM are compared with the results of HFSS Eigenmode Solver (HFSS ES). To study and ensure MMTMM convergence, we have implemented the method in Julia [40] with the possibility of using higher precision arithmetic, with open-source libraries [41], [42]. The number of modes N, retained in the computation has been optimized to provide the best results for each section of the Brillouin zone separately. For the HFSS ES and the MoM, primitive unit cells have been used in simulations. However, since commercial software lacks the ability to directly provide attenuation in the stopband, the validity of the results can only be assessed based on the consistency among the other three modeling methods.

As we study the hexagonal lattices using rectangular supercells, the initial results include extra modes. These extra modes do not provide additional information and can be identified by scanning different parts of the Brillouin zone of the primitive cell, as shown in [25]. Hence, the extra modes are removed from all plots. Furthermore, for clarity of the plots, we only present the modes that have the minimum attenuation in the first stopband.

A. Glide-symmetric holey structure

First, we consider the glide-symmetric structure in Fig. 1. The complete dispersion diagram is presented in Fig. 6(a). For the 2D-MMTMM, 11 modes were used in the x and y ports for the paths $\overline{\Gamma\mathrm{K}_5}$ and $\overline{\mathrm{K}_5\mathrm{K}}$. For path $\overline{\mathrm{K}\mathrm{M}_1}$, 13 modes are used in x and 11 in y ports. For path $\overline{\mathrm{M}_1\Gamma}$, 13 modes are used in x and 9 in y ports. For the 1D-MMTMM,

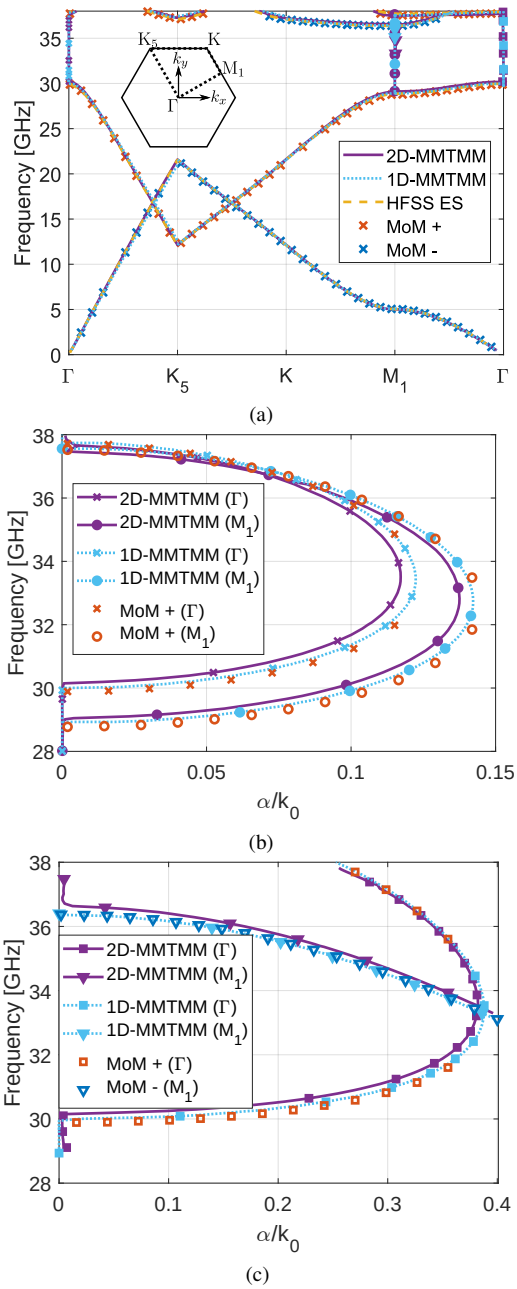

Fig. 6. Results for the optimized glide-symmetric unit cell. (a) Real part of the dispersion diagram. Frequency behavior of the normalized-to-k_0 attenuation constant along (b) the x'-direction and (c) the y'-direction.

10 modes in both x and y were included to resolve all paths. The plus and minus MoM markers refer to solutions obtained with either plus or minus branch of the HSPGF in (35). In Fig. 6(a), excellent agreement is obtained between the four methods. The unit cell has a stopband from 30.1 to 36.4 GHz, making the stopband's fractional bandwidth only about 19%. The normalized attenuation constant in the stopband is shown in Fig. 6(b) for the x'-direction and in Fig. 6(c) for the y'-direction. The unit cell exhibits a strong degree of anisotropy, with a maximum normalized attenuation of about $\alpha/k_0 = 0.12$ in the x'-direction, and a maximum of

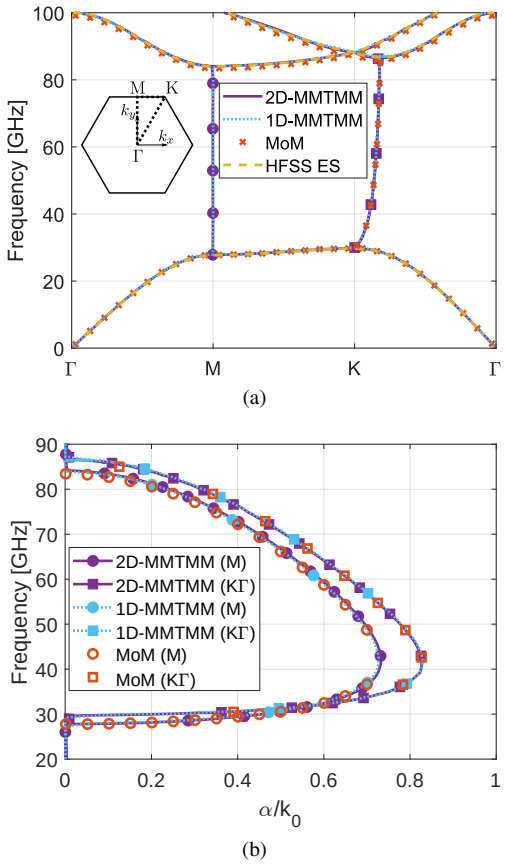

Fig. 7. Results for the optimized MHT unit cell. (a) Real part of the dispersion diagram. (b) Magnitude of the attenuation.

$\alpha/k_0 = 0.38$ in the y'-direction. Here, α is computed as

$$\alpha = \sqrt{\Im\{k_x\}^2 + \Im\{k_y\}^2}\,. \tag{36}$$

The difference in maximum attenuation can be more easily explained with the help of additional information on the mode properties provided by the MoM. Note that the modes of the plus and minus branches of (35) do not transition from one to another, as in rectangular unit cells [30]. Therefore, the mode at the lower frequency bound of the stopband in M_1 in Fig. 6(a) does not transition into a propagative mode at about 36 GHz, as the two propagative modes arise from different branches of the HSPGF. This behavior is more apparent in Fig. 6(c). Because bandwidth and attenuation levels are lower compared to other unit cells [14], [27], and due to its high degree of anisotropy, this specific unit cell does not seem suitable for use as an EBG.

B. Mirror half-turn holey structure

The second unit cell investigated is the MHT structure. The dispersion diagram of the optimized structure is presented in Fig. 7(a). In the 2D-MMTMM, 21, 12, and 16 modes were included in both x and y ports to resolve the paths $\overline{\Gamma\mathrm{M}}$, $\overline{\mathrm{MK}}$, and $\overline{\mathrm{K}\Gamma}$, respectively. For the 1D-MMTMM, 10 modes were included in each port. As before, excellent agreement is obtained among all the methods. The unit cell has a stopband from 29.9 GHz to 83.8 GHz, making a fractional bandwidth

TABLE III
COMPUTATIONAL RESOURCES FOR 10 SAMPLES

Method	Total time [s]	Peak solver memory [MB]
2D-MMTMM	526	510
1D-MMTMM	1310	438
MoM	19147	78

of 94.9%. This is higher than both the glide-symmetric holey unit cell and the three-hole double-layer structure, which have fractional bandwidths of 66.6% and 88.7% [14], respectively. In the stopband, there are two relevant stopband modes, one marked with circles and the other with squares. The latter is a complex mode that connects to the passband at K at the lower frequency and to the lowest point of the second mode in the $\overline{\mathrm{KT}}$ region. The attenuation of the two modes is shown in Fig. 7(b). The stopband attenuation is highly isotropic, with the complex mode reaching slightly higher maximum attenuation than the mode at M.

Since this unit cell appears attractive for practical applications due to its wide bandwidth, we further investigate the effect of varying different parameters in Fig. 8. The left panels of Fig. 8 show the minimum and maximum bounds of the stopband, obtained with HFSS ES, along with the fractional bandwidth. In the right panels of Fig. 8, the minimum stopband attenuation in any direction, obtained with 1D-MMTMM, is presented in color. The results align with earlier research, indicating that enlarging the hole's depth up to approximately half of the period (corresponding to the hexagon's width in this study) enhances the bandwidth. Beyond this point, any further enhancement is marginal [14], [27]. Furthermore, similar to other EBG structures, the gap has a significant inverse correlation with the bandwidth, as illustrated in Fig. 8(c).

C. Computational analysis of the proposed methods

First, we consider the computational resources of each method. For a fair assessment, all computations are performed on a HP ProBook 430 G8 Notebook with Intel i7-1165G7 and 16 GB of RAM. The comparison is given in Table III. The presented times refer to the solution of the eigenproblem for the MHT-symmetric structure. Ten equidistant samples in frequency (for MMTMM), or at different parts of the irreducible Brillouin zone (for the MoM) are used. For both MMTMM approaches, the simulation in CST FDS used 20 modes at the port boundaries while 10 modes were retained to obtain eigenvalues.

Table III shows that both MMTMM methods compare very favorably with respect to the MoM approach for the total computation time, while MoM is much more memory efficient. However, we remark that our in-house MoM code runs on a single thread, while the MMTMM is utilizing a well-optimized and parallelized commercial software. For the MMTMM, the total time includes the setup and resolution of the eigenvalue problem, although this time is negligible compared to the time necessary to obtain the initial scattering matrices.

As a final comment on the usability of the methods, we have found that, in most cases, the 2D-MMTMM is a good starting point for exploring the properties of the structure. It is the fastest among the methods and results in less post-processing work since the entire dispersion diagram is obtained with one simulation. However, we found that the selection of modes is more challenging for the geometries analysed in this paper compared to the 1D-MMTMM approach, especially at higher frequencies. Furthermore, depending on the number of modes included, the resolution of the eigenmode problem can become unstable, resulting in a high condition number of the matrix [43], [44]. This breakdown usually occurs first for the polynomial eigenvalue problem in (23). In this case, solving the problem with quad precision, or using the alternative formulation 1D-MMTMM can help resolve these issues. Ultimately, while MoM (in our in-house implementation) is the slowest among the three methods, it requires the least user input and is thus very robust, so it is a good method to use as a reference.

V. EXPERIMENTAL RESULTS

In order to experimentally test the results obtained numerically, we implemented the MHT structure as an EBG to block the undesired leakage in the interconnection between two rectangular waveguide flanges. For this purpose, we have manufactured four flanges: two standard and two with the mirror-half turn symmetric unit cells implemented as an EBG in the working band of 40-60 GHz of the UG-383/U rectangular waveguide. These flanges are presented in Fig. 9. The parameters of the unit cell [see Fig. 2(b)] are $a = 3$ mm, $r = 0.38a$, and $h = 0.6a$. The shortest distance between the center of the closest hole and the top of the waveguide (longer edge) is 1.44 mm. The geometry on the shorter sides of the waveguide is modified to ensure this distance on both long sides of the waveguide. This modification does not affect the operation of the structure within the designed frequency range, since the leakage occurs mainly from the longer sides of the waveguide.

The measurement setup is presented in Fig. 10(a). The flanges are placed between the ends of two standard coaxial to rectangular waveguide transitions. Different values of the gap between the two plates are achieved using a set of thin metallic spacers. The measured magnitude of the S_{21} parameter of the two prototypes is presented in Fig. 10(b). The effect of the two coaxial to waveguide transitions has been deembedded by using thru-reflect-line (TRL) calibration. The measurements of flanges with the EBG configuration are presented in solid lines, and the flanges without the EBG are presented in dashed lines. The results clearly indicate that increasing the gap increases the losses in the flange without EBG, while the transmitted power is stable when the EBG is present in the structure.

VI. CONCLUSION AND PERSPECTIVES

In this work, we have proposed a MMTMM modelling procedures for periodic structures with a hexagonal lattice. Due to the limitations of the employed commercial solver, which imposes the restriction that the ports must be aligned with the Cartesian axes, we have analyzed a rectangular supercell instead of the primitive hexagonal unit cell. We have

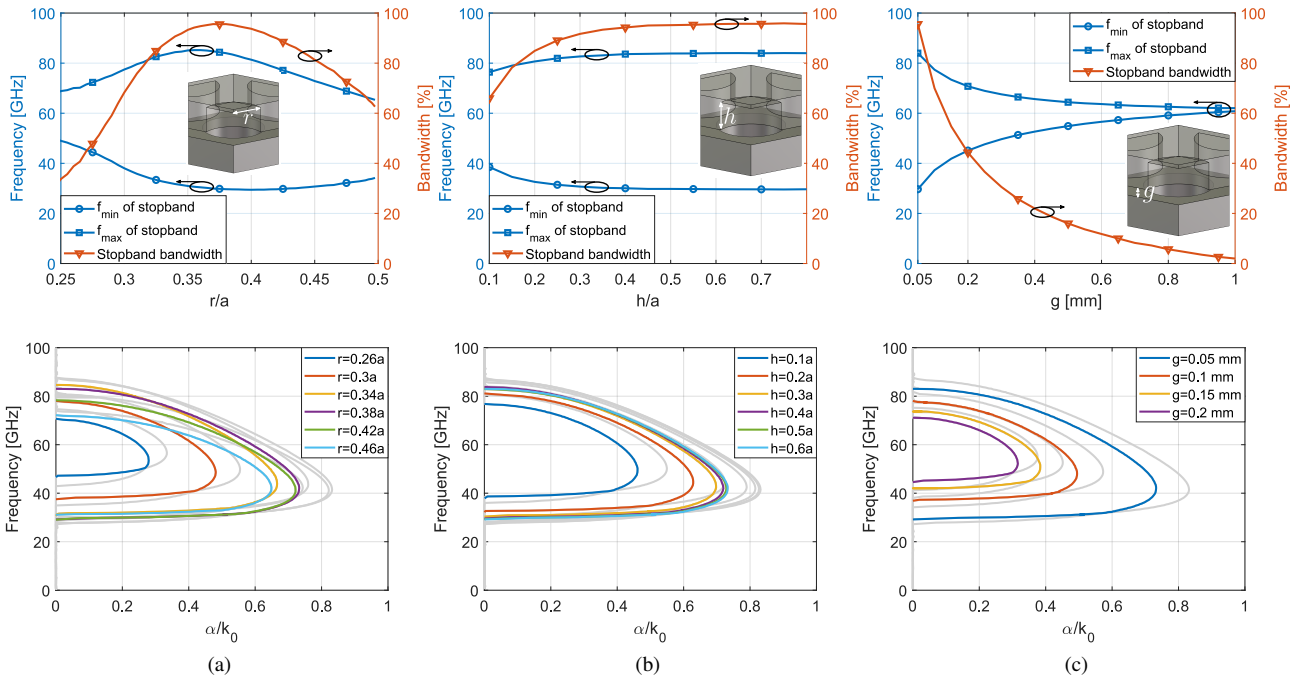

Fig. 8. MHT parameter sweeps. The varied parameters are depicted in the insets. On the top are bounds of the stopband and the fractional bandwidth, and on the bottom is the minimum magnitude of stopband attenuation. (a) Varying the radius of the holes r. (b) Varying the depth of the holes h. (c) Varying the gap between the top and bottom plates g.

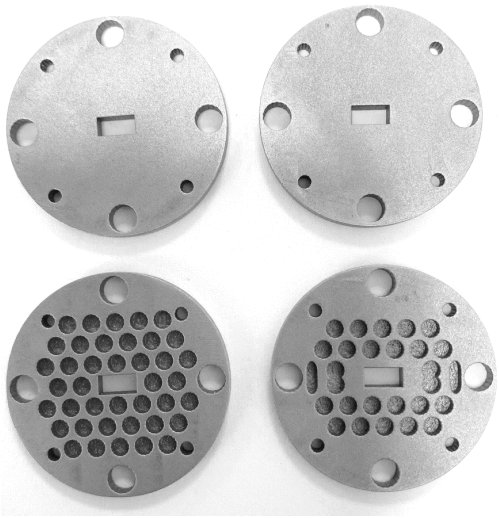

Fig. 9. Manufactured flanges. Without EBG (top) and with the EBG (bottom).

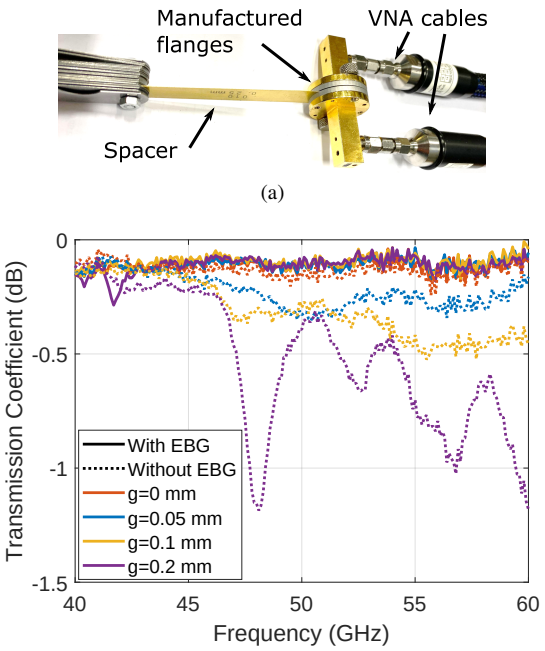

Fig. 10. (a) Measurement setup. The gap is created with a spacer (left). (b) Measured magnitude of S_{21} parameter of the manufactured flanges with different gaps between the flanges with and without EBG.

presented a novel 2D-MMTMM formulation that results in a polynomial eigenvalue problem that is easily solved using companion matrices. We have also presented an alternative 1D-MMTMM approach that involves only two ports and PBCs on the remaining sides of the cell. The results of the proposed MMTMM methods have been compared with the HFSS ES for propagative modes and with the MoM [30] for propagative and stopband modes. We found excellent agreement between all the methods, validating the results of the proposed MMTMM approaches.

Using the modeling approaches presented, we have investigated two cases of hexagonal unit cells with circular holes, one with glide symmetry and one with MHT symmetry. The glide-symmetric unit cell is highly anisotropic and has a small bandwidth in the first stopband, making it unappealing for use as EBG. On the other hand, the first stopband of

the symmetric unit cell MHT is wideband, with a fractional bandwidth of 94.9%. We have validated its usefulness as EBG by additively manufacturing flanges and studied its ability to block undesired leakage in interconnections.

Other comprehensive investigation into a broad range of hexagonal unit cells using the methods described in this study is feasible and will be the aim of future works.

ACKNOWLEDGMENT

The authors would like to thank Dr. Qiao Chen for helpful discussions and providing simulation files for the spacers from [14].

APPENDIX A

In this appendix, we provide the complete derivation of the polynomial MMTMM formulation (13). We start writing the permuted matrix eigenvalue problem

$$\begin{bmatrix}[\widetilde{\mathbf{T}}_{xx}] & [\widetilde{\mathbf{T}}_{xy}]\\ [\widetilde{\mathbf{T}}_{yx}] & [\widetilde{\mathbf{T}}_{yy}]\end{bmatrix}\begin{bmatrix}\mathbf{F}_x\\ \mathbf{F}_y\end{bmatrix}=\begin{bmatrix}\lambda_x\mathbf{F}_x\\ \lambda_y\mathbf{F}_y\end{bmatrix} \tag{37}$$

as

$$[\widetilde{\mathbf{T}}_{xx}]\mathbf{F}_x+[\widetilde{\mathbf{T}}_{xy}]\mathbf{F}_y=\lambda_x\mathbf{F}_x \tag{38}$$

$$[\widetilde{\mathbf{T}}_{yx}]\mathbf{F}_x+[\widetilde{\mathbf{T}}_{yy}]\mathbf{F}_y=\lambda_y\mathbf{F}_y\ . \tag{39}$$

Now, we assume the phases are interdependent as

$$\varphi_y=n\varphi_x+\varphi_{y0} \tag{40}$$

or, following (12), equivalent to

$$\lambda_y=\lambda_x^n\lambda_{y0}\ . \tag{41}$$

In this case, (39) can be rewritten as

$$[\widetilde{\mathbf{T}}_{yx}]\mathbf{F}_x+[\widetilde{\mathbf{T}}_{yy}]\mathbf{F}_y=\lambda_x^n\lambda_{y0}\mathbf{F}_y \tag{42}$$

from which $\mathbf{F}_y$ can be expressed as

$$\mathbf{F}_y=\big(\lambda_x^n\lambda_{y0}[\mathbf{I}]-[\widetilde{\mathbf{T}}_{yy}]\big)^{-1}[\widetilde{\mathbf{T}}_{yx}]\mathbf{F}_x\ . \tag{43}$$

If we now insert (43) into (38),

$$\begin{aligned}&[\widetilde{\mathbf{T}}_{xx}]\mathbf{F}_x\\ &\quad+[\widetilde{\mathbf{T}}_{xy}]\big(\lambda_x^n\lambda_{y0}[\mathbf{I}]-[\widetilde{\mathbf{T}}_{yy}]\big)^{-1}[\widetilde{\mathbf{T}}_{yx}]\mathbf{F}_x=\lambda_x\mathbf{F}_x\end{aligned} \tag{44}$$

and left-multiplying (44) by $\big([\mathbf{I}]\lambda_x^n\lambda_{y0}-[\widetilde{\mathbf{T}}_{yy}]\big)[\widetilde{\mathbf{T}}_{xy}]^{-1}$, after merging common powers of λ_x, the equation can be rearranged in the form given in (13), here given in the expanded form

$$\begin{aligned}\Big([\widetilde{\mathbf{T}}_{xy}]^{-1}\lambda_{y0}\lambda_x^{n+1}&-[\widetilde{\mathbf{T}}_{xy}]^{-1}[\widetilde{\mathbf{T}}_{xx}]\lambda_{y0}\lambda_x^n\\ &-[\widetilde{\mathbf{T}}_{yy}][\widetilde{\mathbf{T}}_{xy}]^{-1}\lambda_x+[\widetilde{\mathbf{T}}_{yy}][\widetilde{\mathbf{T}}_{xy}]^{-1}[\widetilde{\mathbf{T}}_{xx}]\\ &-[\widetilde{\mathbf{T}}_{yx}]\Big)\mathbf{F}_x=[\mathbf{0}]\ .\end{aligned} \tag{45}$$

For completeness, we also provide the analogous MMTMM formulation when the relation between φ_x and φ_y is

$$\varphi_x=n\varphi_y+\varphi_{x0} \tag{46}$$

or, equivalently,

$$\lambda_x=\mathrm{e}^{-\mathrm{j}n\varphi_y}\mathrm{e}^{-\mathrm{j}\varphi_{x0}}=\lambda_y^n\lambda_{x0}\ . \tag{47}$$

In this case, we find the following polynomial MMTMM form:

$$\big([\mathbf{M}_{n+1,y}]\lambda_y^{n+1}+[\mathbf{M}_{n,y}]\lambda_y^n+[\mathbf{M}_{1,y}]\lambda_y+[\mathbf{M}_{0,y}]\big)\mathbf{F}_y=[\mathbf{0}] \tag{48}$$

with

$$[\mathbf{M}_{n+1,y}]=\lambda_{x0}[\widetilde{\mathbf{T}}_{yx}]^{-1} \tag{49}$$

$$[\mathbf{M}_{n,y}]=-\lambda_{x0}[\widetilde{\mathbf{T}}_{yx}]^{-1}[\widetilde{\mathbf{T}}_{yy}] \tag{50}$$

$$[\mathbf{M}_{1,y}]=-[\widetilde{\mathbf{T}}_{xx}][\widetilde{\mathbf{T}}_{yx}]^{-1} \tag{51}$$

$$[\mathbf{M}_{0,y}]=[\widetilde{\mathbf{T}}_{xx}][\widetilde{\mathbf{T}}_{yx}]^{-1}[\widetilde{\mathbf{T}}_{yy}]-[\widetilde{\mathbf{T}}_{xy}]\ . \tag{52}$$

REFERENCES

[1] W. Jiang, B. Han, M. A. Habibi, and H. D. Schotten, "The Road Towards 6G: A Comprehensive Survey," *IEEE Open J. Commun. Soc.*, vol. 2, pp. 334–366, 2021.

[2] O. Quevedo-Teruel, Q. Chen, F. Mesa, N. J. Fonseca, and G. Valerio, "On the Benefits of Glide Symmetries for Microwave Devices," *IEEE J. Microw.*, vol. 1, no. 1, pp. 457–469, 2021.

[3] F. Ghasemifard, M. Norgren, and O. Quevedo-Teruel, "Twist and polar glide symmetries: an additional degree of freedom to control the propagation characteristics of periodic structures," *Sci. Rep.*, vol. 8, no. 1, p. 11266, 2018.

[4] P. Crepeau and P. R. McIsaac, "Consequences of symmetry in periodic structures," *Proc. IEEE*, vol. 52, no. 1, pp. 33–43, 1964.

[5] R. Mittra and S. Laxpati, "Propagation in a wave guide with glide reflection symmetry," *Canadian J. Phys.*, vol. 43, no. 2, pp. 353–372, 1965.

[6] A. Hessel, M. H. Chen, R. C. Li, and A. A. Oliner, "Propagation in periodically loaded waveguides with higher symmetries," *Proc. IEEE*, vol. 61, no. 2, pp. 183–195, 1973.

[7] O. Quevedo-Teruel, J. Miao, M. Mattsson, A. Algaba-Brazalez, M. Johansson, and L. Manholm, "Glide-Symmetric Fully Metallic Luneburg Lens for 5G Communications at Ka-Band," *IEEE Antennas Wireless Propag. Lett.*, vol. 17, no. 9, pp. 1588–1592, 2018.

[8] W. Yuan, J. F. Chen, C. Zhang, W. X. Tang, L. Wang, Q. Cheng, and T. J. Cui, "Glide-Symmetric Lens Antenna in Gap Waveguide Technology," *IEEE Trans. Antennas Propag.*, vol. 68, no. 4, pp. 2612–2620, 2020.

[9] G. Zhang, Q. Zhang, Y. Chen, and R. D. Murch, "High-scanning-rate and wide-angle leaky-wave antennas based on glide-symmetry Goubau line," *IEEE Trans. Antennas Propag.*, vol. 68, no. 4, pp. 2531–2540, 2019.

[10] Q. Chen, O. Zetterstrom, E. Pucci, A. Palomares-Caballero, P. Padilla, and O. Quevedo-Teruel, "Glide-symmetric holey leaky-wave antenna with low dispersion for 60 GHz point-to-point communications," *IEEE Trans. Antennas Propag.*, vol. 68, no. 3, pp. 1925–1936, 2019.

[11] S. Lei, G. Wei, K. Han, and M. Wang, "Simple method to suppress n=- 2 harmonic for periodic leaky-wave antennas with open-stopband suppression," *J. Phys. D Appl. Phys.*, vol. 56, no. 47, p. 475002, 2023.

[12] M. Ebrahimpouri, E. Rajo-Iglesias, Z. Sipus, and O. Quevedo-Teruel, "Cost-Effective Gap Waveguide Technology Based on Glide-Symmetric Holey EBG Structures," *IEEE Trans. Microw. Theory Techn.*, vol. 66, no. 2, pp. 927–934, 2018.

[13] M. Ebrahimpouri, A. Algaba Brazalez, L. Manholm, and O. Quevedo-Teruel, "Using Glide-Symmetric Holes to Reduce Leakage Between Waveguide Flanges," *IEEE Microw. Wireless Compon. Lett.*, vol. 28, no. 6, pp. 473–475, 2018.

[14] L. F. Herran, Q. Chen, F. Mesa, and O. Quevedo-Teruel, "Electromagnetic Bandgap Based on a Compact Three-Hole Double-Layer Periodic Structure," *IEEE Trans. Antennas Propag.*, vol. 72, no. 1, pp. 1045–1050, 2024.

[15] Z. Sipus, K. Cavar, M. Bosiljevac, and E. Rajo-Iglesias, "Glide-symmetric holey structures applied to waveguide technology: Design considerations," *Sensors*, vol. 20, no. 23, p. 6871, 2020.

[16] E. Rajo-Iglesias, A. U. Zaman, and P.-S. Kildal, "Parallel Plate Cavity Mode Suppression in Microstrip Circuit Packages Using a Lid of Nails," *IEEE Microw. Wireless Compon. Lett.*, vol. 20, no. 1, pp. 31–33, 2010.

[17] D. Sun, X. Chen, J.-Y. Deng, L.-X. Guo, W. Cui, K. Yin, Z. Chen, C. Yao, and F. Huang, "Gap Waveguide With Interdigital-Pin Bed of Nails for High-Frequency Applications," *IEEE Trans. Microw. Theory Tech.*, vol. 67, no. 7, pp. 2640–2648, 2019.

[18] D. Sievenpiper, L. Zhang, R. Broas, N. Alexopolous, and E. Yablonovitch, "High-impedance electromagnetic surfaces with a forbidden frequency band," *IEEE Trans. Microw. Theory Tech.*, vol. 47, no. 11, pp. 2059–2074, 1999.

[19] W. Tan, Y. He, H. Luo, G. Zhao, and H. Sun, "Low-Cost Gap Waveguide Technology Using Shallow Grooves and Glide-Symmetric Semicircular-Holes EBG Structures," *IEEE Antennas Wireless Propag. Lett.*, vol. 22, no. 12, pp. 2901–2905, 2023.

[20] J. D. de Pineda, A. P. Hibbins, and J. R. Sambles, "Microwave edge modes on a metasurface with glide symmetry," *Phys. Rev. B*, vol. 98, p. 205426, Nov 2018.

[21] S. Yang, O. Zetterstrom, Z. Xue, F. Mesa, and O. Quevedo-Teruel, "Hexagonal higher-symmetric dielectric periodic structures for planar graded-index lenses," *Appl. Phys. Lett.*, vol. 123, no. 1, p. 011707, 07 2023.

[22] K. C. Chen, J. W. Yang, Y.-C. Yang, C. F. Khin, and M. N. M. Kehn, "Plasmonic Luneburg lens antenna synthesized by metasurfaces with hexagonal lattices," *Opt. Express*, vol. 25, no. 22, pp. 27 405–27 414, Oct 2017.

[23] O. Kiris, K. Topalli, and M. Unlu, "A Reflectarray Antenna Using Hexagonal Lattice With Enhanced Beam Steering Capability," *IEEE Access*, vol. 7, pp. 45 526–45 532, 2019.

[24] Y.-J. Park and W. Wiesbeck, "Angular independency of a parallel-plate Luneburg lens with hexagonal lattice and circular metal posts," *IEEE Antennas Wireless Propag. Lett.*, vol. 1, pp. 128–130, 2002.

[25] S. Yang, O. Zetterstrom, F. Mesa, and O. Quevedo-Teruel, "Dispersion Analysis of Metasurfaces With Hexagonal Lattices With Higher Symmetries," *IEEE J. Microw.*, vol. 3, no. 4, pp. 1154–1165, 2023.

[26] A. Barlevy and Y. Rahmat-Samii, "Characterization of electromagnetic band-gaps composed of multiple periodic tripods with interconnecting vias: concept, analysis, and design," *IEEE Trans. Antennas Propag.*, vol. 49, no. 3, pp. 343–353, 2001.

[27] Q. Chen, F. Mesa, X. Yin, and O. Quevedo-Teruel, "Accurate Characterization and Design Guidelines of Glide-Symmetric Holey EBG," *IEEE Trans. Microw. Theory Techn.*, vol. 68, no. 12, pp. 4984–4994, 2020.

[28] D. Tomić and Z. Šipuš, "Rigorous Coupled Wave Analysis of Parallel-Plate Waveguides Loaded With Glide-Symmetric Dielectric Structures," *IEEE Trans. Microw. Theory Techn.*, pp. 1–13, 2024.

[29] S. Amari, R. Vahldieck, and J. Bornemann, "Accurate analysis of periodic structures with an additional symmetry in the unit cell from classical matrix eigenvalues," *IEEE Trans. Microw. Theory Techn.*, vol. 46, no. 10, pp. 1513–1515, 1998.

[30] M. Petek, J. Rivero, J. A. T. Vásquez, G. Valerio, O. Quevedo-Teruel, and F. Vipiana, "Method of Moments for the Dispersion Modeling of Glide-Symmetric Periodic Structures," *IEEE Trans. Antennas Propag.*, vol. 72, no. 1, pp. 756–766, 2024.

[31] F. Mesa, G. Valerio, R. Rodriguez-Berral, and O. Quevedo-Teruel, "Simulation-Assisted Efficient Computation of the Dispersion Diagram of Periodic Structures: A comprehensive overview with applications to filters, leaky-wave antennas and metasurfaces," *IEEE Antennas Propag. Mag.*, vol. 63, no. 5, pp. 33–45, 2020.

[32] F. Giusti, Q. Chen, F. Mesa, M. Albani, and O. Quevedo-Teruel, "Efficient Bloch Analysis of General Periodic Structures With a Linearized Multimodal Transfer-Matrix Approach," *IEEE Trans. Antennas Propag.*, vol. 70, no. 7, pp. 5555–5562, 2022.

[33] M. Petek, J. A. T. Vasquez, G. Valerio, F. Mesa, O. Quevedo-Teruel, and F. Vipiana, "Efficient Numerical Computation of Dispersion Diagrams for Glide-Symmetric Periodic Structures with a Hexagonal Lattice," in *2024 18th European Conference on Antennas and Propagation (EuCAP)*, 2024, pp. 1–5.

[34] F. Tisseur, "Backward error and condition of polynomial eigenvalue problems," *Linear Algebra Appl.*, vol. 309, no. 1, pp. 339–361, 2000.

[35] N. J. Higham, D. S. Mackey, and F. Tisseur, "The Conditioning of Linearizations of Matrix Polynomials," *SIAM J. Matrix Anal. Appl.*, vol. 28, no. 4, pp. 1005–1028, 2006.

[36] S. Yang, F. Mesa, O. Zetterstrom, S. Clendinning, and O. Quevedo-Teruel, "Understanding the Dispersion Diagrams of Two-Dimensional Supercells," in *2022 Microwave Mediterranean Symposium (MMS)*, 2022, pp. 1–4.

[37] J. D. Joannopoulos, S. G. Johnson, J. N. Winn, and R. D. Meade, *Photonic Crystals*. Princeton: Princeton University Press, 2008, ch. 3. Accessed: June 26, 2024. [Online]. Available: https://doi.org/10.1515/9781400828241

[38] M. Bagheriasl, O. Quevedo-Teruel, and G. Valerio, "Bloch Analysis of Artificial Lines and Surfaces Exhibiting Glide Symmetry," *IEEE Trans. Microw. Theory Techn.*, vol. 67, no. 7, pp. 2618–2628, 2019.

[39] F. T. Celepcikay, D. R. Wilton, D. R. Jackson, and F. Capolino, "Choosing splitting parameters and summation limits in the numerical evaluation of 1-D and 2-D periodic Green's functions using the Ewald method," *Radio Sci.*, vol. 43, no. 06, pp. 1–11, 2008.

[40] J. Bezanson, A. Edelman, S. Karpinski, and V. B. Shah, "Julia: A Fresh Approach to Numerical Computing," *SIAM Review*, vol. 59, no. 1, pp. 65–98, 2017. Accessed October 14, 2024. [Online]. Available: https://doi.org/10.1137/141000671

[41] D. K. Zhang and et al., "Fast, SIMD-accelerated extended-precision arithmetic for julia," Oct 2019. [Online]. Available: https://github.com/dzhang314/MultiFloats.jl

[42] A. Noack and et al., "Generic numerical linear algebra in julia," Dec 2018. [Online]. Available: https://github.com/JuliaLinearAlgebra/GenericLinearAlgebra.jl

[43] W. Best, R. Riegert, and L. Goodrich, "Dispersion analysis of the linear vane-type waveguide using the generalized scattering matrix," *IEEE Trans. Microw. Theory Techn.*, vol. 43, no. 9, pp. 2101–2108, 1995.

[44] F. Bongard, J. Perruisseau-Carrier, and J. R. Mosig, "Enhanced Periodic Structure Analysis Based on a Multiconductor Transmission Line Model and Application to Metamaterials," *IEEE Trans. Microw. Theory Techn.*, vol. 57, no. 11, pp. 2715–2726, 2009.